

# **Supporting Information for**

## **Measuring Nanoparticle Polarizability using Fluorescence Microscopy**

*Wenhan Cao,<sup>1</sup> Margaret Chern,<sup>2</sup> Allison M. Dennis,<sup>2,3</sup> and Keith A. Brown<sup>1,2,4,\*</sup>*

<sup>1</sup>Department of Mechanical Engineering, Boston University, Boston, MA, 02215, USA

<sup>2</sup>Division of Materials Science & Engineering, Boston University, Boston, MA, 02215, USA

<sup>3</sup>Department of Biomedical Engineering, Boston University, Boston, MA, 02215, USA

<sup>4</sup>Physics Department, Boston University, Boston, MA, 02215, USA

<b><u>1. MATERIALS AND METHODS</u></b>	<b>2</b>
<b>1.1 Synthesis of Quantum Dots</b>	<b>2</b>
<b>1.2 Quantum Dot Core Size Determination</b>	<b>4</b>
<b>1.3 Borate Buffer Preparation</b>	<b>5</b>
<b>1.4 Fabrication of Microfluidic Chamber</b>	<b>5</b>
<b>1.5 Optical Microscopy</b>	<b>6</b>
<b><u>2. THEORY AND ANALYSIS</u></b>	<b>7</b>
<b>2.1. Modeling the Electric Field in the Electrode Array</b>	<b>7</b>
<b>2.2. Quantifying Concentration and Polarizability</b>	<b>13</b>
<b><u>3. SUPPORTING REFERENCES</u></b>	<b>18</b>

## **1. MATERIALS AND METHODS**

### **1.1 Synthesis of Quantum Dots**

#### ***CdSe Cores***

CdSe cores were synthesized in a procedure adapted by Chern *et. al*<sup>1</sup> from Ghosh *et. al*.<sup>2</sup> 1 g of trioctylphosphine oxide (TOPO), 1.9 mL of 0.2 M cadmium oleate (Cd(OA)<sub>2</sub>) in octadecene (ODE) (0.38 mmol), and 8 mL of ODE were loaded in a 100 mL round bottom flask (rbf) attached to a Schlenk line and degassed under vacuum for 30 min at room temperature. The solution was heated to 80 °C under vacuum for an additional 30 min to ensure air-free reaction conditions. The flask was filled with Ar and heated to 300 °C. Once the solution reached 300 °C, a solution consisting of 4 mL 1 M trioctylphosphine (TOP):Se, 3 mL oleylamine (Olam), and 1 mL ODE was quickly injected and the reaction temperature set to 270 °C for growth. The solution was annealed at 270 °C for 3 min before the flask was removed from the heating mantle to cool to room temperature. The cores were cleaned in a glovebox (Ar) by precipitation with ethanol and methanol and resuspended in hexanes for storage.

#### ***CdS Shelling***

We deposited CdS shells on CdSe cores by modifying a previously reported protocol by Nasilowski *et. al*.<sup>3</sup> For QDs with a diameter of 15 nm (analysis by TEM), 120 nmol of CdSe cores were loaded into a 100 mL rbf with 5 mL of ODE, 2 mL of Olam, and 120 mg of myristic acid. The solution was heated to 70 °C and held under vacuum for 30 min before heating to 260 °C under Ar. The solution was kept at 260 °C for 20 min before 4.5 mL of a pre-mixed Cd/S precursor consisting of 0.9 M Cd(OA)<sub>2</sub> and 0.8 M S diluted in ODE was injected at a rate of 2.25 mL/hr *via* syringe pump. Once injection was complete (2 hr) the reaction was heated to 310 °C and an

additional 10 mL of the Cd/S solution described above was injected at 5 mL/hr. The solution was allowed to anneal for an additional 4 hr after the injection was complete.

### ***PMAO coating***

An amphiphilic polymer, poly(maleic anhydride-*alt*-1-octadecene) (PMAO), was used to impart water solubility to the synthesized QDs through modification of a protocol reported by Corato *et. al.*<sup>4</sup> QDs were first precipitated from their original reaction solution using ethanol and methanol and resuspended in chloroform. PMAO was dissolved in chloroform (0.137 M, by monomer) and added to the QDs so that there were 500 monomers per nm<sup>2</sup> of QD surface area. The solution was diluted with chloroform to a final QD concentration of 100 nM. The QD/PMAO solution was slowly evaporated to dryness using a rotary evaporator. Once a dry film of QDs/PMAO formed, 0.2 M bis(hexamethylene)triamine in chloroform was added such that there were 10 triamine molecules per nm<sup>2</sup> of QD surface area. Chloroform was added to bring the final QD concentration to 500 nM. The solution was sonicated at room temperature for 30 min before evaporating to dryness. The QD/PMAO film was recovered in 1× borate buffer through sonication at 60 °C until the solution was colored and clear (1-4 hrs). The resulting solution was filtered through 0.45 and 0.22 µm polyethersulfone (PES) syringe filters before ultra-centrifugation on a 20 - 60% sucrose gradient made with 5% step sizes. Samples were ultracentrifuged at 45,000 RPM at 4 °C for 4 hr to separate QDs from free polymer. The QD band was extracted from the gradient and buffer exchanged by spin filtration into 1× borate buffer for storage. Borate concentration was adjusted through dilution with DI H<sub>2</sub>O or addition of 20× borate buffer immediately prior to DEP experiments.

## 1.2 Quantum Dot Core Size Determination

### *Dynamic Light Scattering (DLS)*

The hydrodynamic size of QD samples was measured by Zetasizer Nano ZS90 based on dynamic light scattering (DLS). 50  $\mu\text{L}$  of 25 nM QD was pipetted into ZEN0118 disposable low volume polystyrene cuvette and put in the cell holder. The sample was equilibrated for 1 min and set to 25  $^{\circ}\text{C}$  at a  $90^{\circ}$  scattering angle. We report the average hydrodynamic size of the particles from 12 measurements of a single sample.

### *Negative stain transmission electron microscopy (TEM)*

Uncoated QDs were cleaned  $2\times$  via precipitation with ethanol/methanol and dilute resuspension in chloroform for TEM imaging. PMAO-coated QDs were prepared for TEM with a negative stain to visualize the polymer coating surrounding the semiconductor core. After the concentrated QD stock was diluted 1:100 in deionized water, a drop (5-10  $\mu\text{L}$ ) was placed on parafilm. A 400 mesh copper TEM grid with carbon film (Electron Microscopy Sciences) was placed copper side down on the sample droplet for 5-10 min before the grid was removed and dried by wicking with filter paper. Once the grid was completely dry, a drop of UranyLess (EMS 22409) was placed on the parafilm and the grid placed on top for  $\sim 1$  min. The grid was again dried by wicking with filter paper. TEM imaging was performed at Center for Nanoscale Systems (CNS), using a Jeol 2100 TEM, operating at 200 kV.

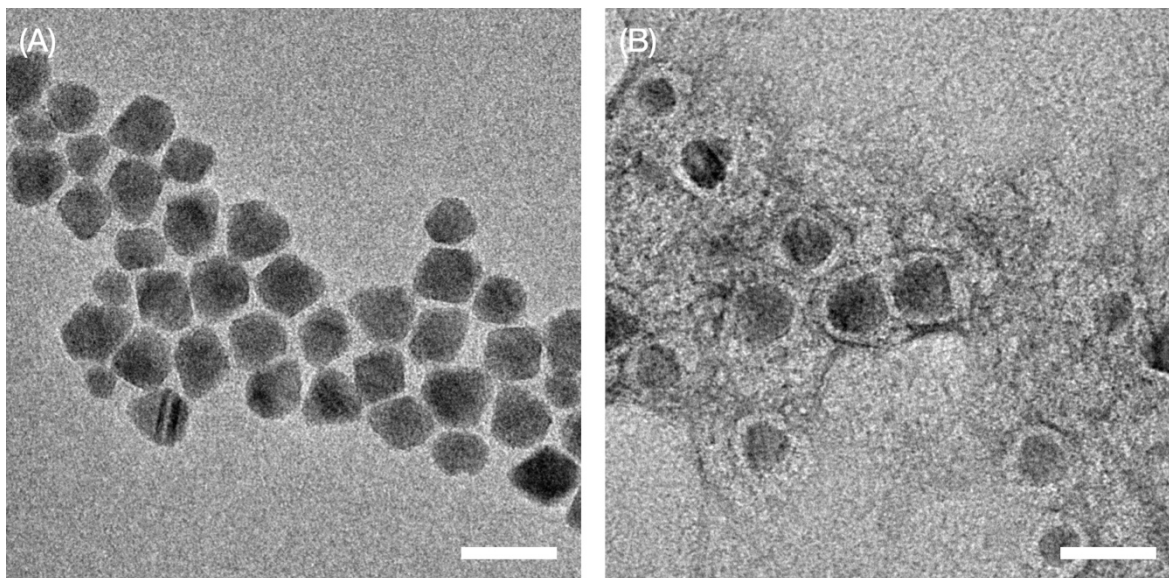


**Figure S1. Transmission electron microscopy (TEM) of QDs (A) before and (B) after coating with PMAO.** A negative stain is used in (B) to reveal the width of the polymeric shell. Scale bars are 25 nm.

### 1.3 Borate buffer preparation

QDs were stored in 1× borate buffer (50 mM borate buffer, pH 8.5, Thermo Fisher Scientific) and diluted to a final QD concentration of 25 nM with either DI H<sub>2</sub>O or borate buffer to obtain final borate concentrations of: 50, 12.5, and 3.125 mM. A VWR symphony H10C handheld meter was employed to measure the conductivity of the buffer solution at room temperature (25 °C) (Table S1).

### 1.4 Fabrication of Microfluidic Chamber

To make a microfluidic chamber for the polarizability assay, we began by etching a series of electrodes onto an indium tin oxide (ITO)-coated glass slide (Figure S2). Briefly, a 25 × 75 mm<sup>2</sup> glass slide that had been coated with ITO (University wafers) was coated with AZ 5214E photoresist. Then, photolithography was performed and part of the photoresist was removed using MF-319 developer leaving the interleaved electrodes uncovered. A layer of 50 nm thick Cr was

evaporated onto the ITO slide using an Angstrom engineering coater. After deposition, residual photoresist was removed by sonication in acetone and IPA. The exposed ITO was removed using Plasma-Therm® 790 reactive ion etcher with Ar at a flow rate of 5 sccm, a chamber pressure of 10 mTorr, and power of 200 W for 15 min. After removal of the Cr mask using a Cr-etchant, the ITO electrodes were ready for use. To make a spacer to define the height of the microfluidic chamber, S1818 photoresist was spin-coated on the electrodes and subjected to photolithography and subsequent development.

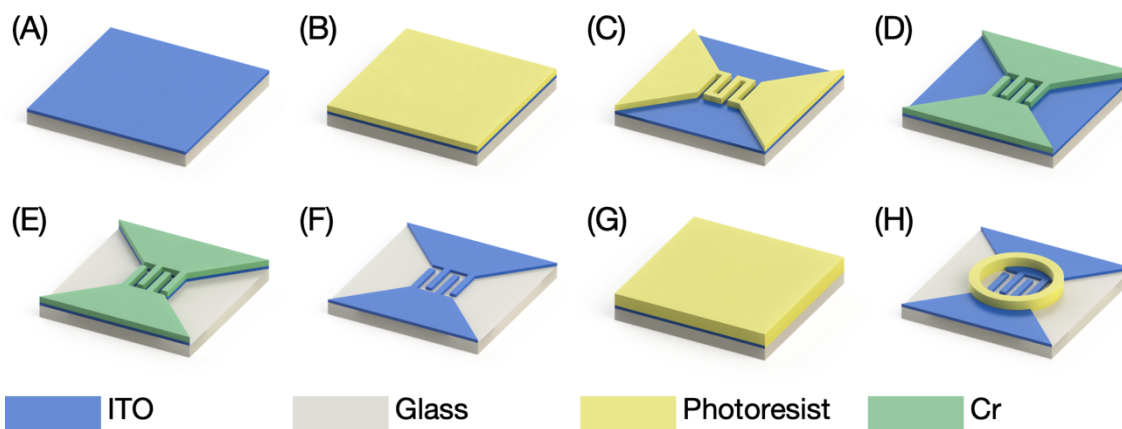


**Figure S2. Fabrication process of indium tin oxide (ITO) electrode arrays and microfluidic chamber.** (A)  $25 \times 75 \text{ mm}^2$  ITO-coated glass slide. (B) AZ 5214E photoresist was spin-coated on the ITO surface. (C) Photoresist partially removed using photolithography and development. (D) Cr evaporated onto ITO slides and then residual photoresist was removed using lift-off. (E) Exposed ITO removed by reactive ion etching (RIE). (F) Remaining chrome removed. (G) S1818 Photoresist was spin-coated and a (H) spacer was defined using photolithography and subsequent development.

### 1.5 Optical Microscopy

Fluorescence images were taken using Hamamatsu ORCA R2 camera with resolution of  $1344 \times 1024$  pixels on an Olympus BX43 microscope with a  $20\times$  objective on an optical table to minimize vibrations. The camera was set to have a 15 dB gain and a 500 ms exposure time to allow for sufficient contrast. In order to ensure a linear brightness vs. concentration relationship, gamma was set to 1. The sample was illuminated with an X-Cite® 120Q wide-field fluorescence

microscope excitation light source. A custom filter cube was utilized with an emission wavelength at 642 nm, 75 nm BW (67-036 – Edmund Optics Inc.), a shortpass excitation filter a cutoff at 500 nm (84-706 – Edmund Optics Inc.), and a dichroic cutoff at 550 nm (DMLP550R – ThorLabs Inc.). A Keysight 33521B waveform generator was employed to provide a sinusoidal voltage to the microelectrodes.

In a typical experiment, 5  $\mu\text{L}$  of QD solution was pipetted onto the center of the electrodes, and a  $25 \times 25 \text{ mm}^2$  glass coverslip placed on top of the photoresist spacer, forming a fluid cell. Between each measurement, the waveform generator was kept off for 1 min to allow the QDs to disperse and become uniformly distributed in the fluid cell again before the next measurement.

## **2. THEORY AND ANALYSIS**

### **2.1. Modeling the Electric Field in the Electrode Array**

In order to confidently analyze the relationship between the motion of QDs and applied voltages, it is critical that we know the local field  $E$  that arises from an applied voltage  $V$ . There are two major barriers to this: (1)  $E$  is dictated by the voltage across the medium  $V_m$ , which likely differs from  $V$  due to loss in different parts of the system, and (2) even knowing  $V_m$ ,  $E$  must be computed based upon the specific geometry of the electrodes. To address these challenges, we employ combination of finite element analysis (FEA) and lumped element analysis of the circuit array.

#### ***Lumped Element Model of Microfluidic System***

In order to analyze the operation of this system, we constructed a lumped element circuit model of this system that includes the series resistance of the leads  $R_e$ , electrode polarization

induced electric double layer capacitance  $C_e$ , medium resistance  $R_m$ , and medium capacitance  $C_m$  (Figure 2E). This model serves two important purposes, (1) it allows the total impedance  $Z_s$  of the system to be estimated, which is,

$$Z_s = 2(R_e + \frac{1}{j\omega C_e}) + \frac{R_m}{j\omega C_m R_m + 1}, \quad (\text{S1})$$

where  $f$  is the operating frequency, and it allows the ratio  $V_m/V$  to be estimated which is,

$$\left| \frac{V_m}{V} \right| = \left| \frac{j\omega C_e R_m}{2(j\omega C_e R_e + 1)(j\omega C_m R_m + 1) + R_m} \right|. \quad (\text{S2})$$

Critically, we seek to identify conditions for which  $V_m \approx V$  such that the electric field in the microfluidic device is consistent with the applied voltage. In order to do this, we must determine estimates for the values of the lumped element parameters.

Electrode capacitance  $C_e$  is estimated to be,<sup>5</sup>

$$C_e \sim \frac{\epsilon_m A}{\lambda_D}, \quad (\text{S3})$$

where  $\epsilon_m$  is the permittivity of the medium,  $A$  is the top surface area of the interdigitated ITO electrode fingers (as designed in the photomask), and Debye length  $\lambda_D$  due to electric double layer is given by,

$$\lambda_D = \sqrt{\frac{\epsilon_m k_B T}{2 N_A e^2 I}}, \quad (\text{S4})$$

where  $I$  is the ionic strength of the electrolyte,  $k_B$  is the Boltzmann constant,  $T$  is the absolute temperature in Kelvin,  $N_A$  is Avogadro's number, and  $e$  is the elementary charge. This assumption effectively treats electrode polarization as a parallel plate capacitor whose thickness is given by  $\lambda_D$ . While Equation (S3) is an approximation and could be improved upon through detailed simulations that take into account free and bound charge in the medium, this approximation predicts that the acceptable frequency range extends two orders of magnitude above and below the



working frequency of 1 MHz (Figure 2E), suggesting that refinements to the estimate will not affect the outcome of this analysis.

In order to estimate an upper bound for the electrode resistance  $R_e$ , the geometry of the electrode array was combined with the  $10 \Omega/\square$  sheet resistance measured for these ITO films to find  $R_e \lesssim 450 \Omega$  (including  $50 \Omega$  output impedance of waveform generator).

### ***Finite Element Simulations to Determine Field Profile and Lumped Element Values***

In order to accurately simulate the field profile in the microfluidic device, we characterized the surface profile of the electrode arrays using a Zygo optical surface profiler and Asylum Research MFP-3D Infinity atomic force microscope. After measuring the surface structure, the geometry was imported into COMSOL Multi-physics 5.1 and electric fields in the vicinity of the interdigitated electrode device were simulated in the electrostatic limit (Figure S3). The electrostatic limit applies when all charges are stationary and the current is zero. In particular, Maxwell's equations become,

$$\nabla^2 \phi = -\frac{\rho}{\epsilon_m}, \quad (\text{S5})$$

where  $\phi$  is electrostatic potential field,  $\rho$  is charge density,  $\epsilon_m$  is the medium permittivity. Solving this type of Poisson's equation is fast and routine in finite element solvers such as COMSOL. Here, we simulate the 2D region corresponding to the space corresponding to two electrode gaps (Figure S3). In order to establish boundary conditions, we employ fixed voltages on electrodes (Dirichlet) and periodic boundary conditions on the left and right edges, to reflect the symmetry of the electrode array. The field at the top and bottom was constrained using a no-field condition (Neumann). While this is not strictly physical, the top and bottom glass regions were made thicker (20-100  $\mu\text{m}$ ) until the capacitance of the system and field profile in the water region did not

appreciably change. It is important to note that the electrode polarization region does not explicitly enter into these calculations and will enter into the lumped element model through a discrete lumped element. Indeed, since  $\lambda_D$  is so much smaller than all geometric factors in this system, the only effect of electrode polarization is to reduce the electrode voltage  $V_m$  relative to the applied voltage  $V$ , which is explicitly treated by modeling  $R_e$  and  $C_e$ . The glass was modeled as being electrically insulating with a permittivity of  $2.09\epsilon_0$  where  $\epsilon_0$  is the permittivity of free space.

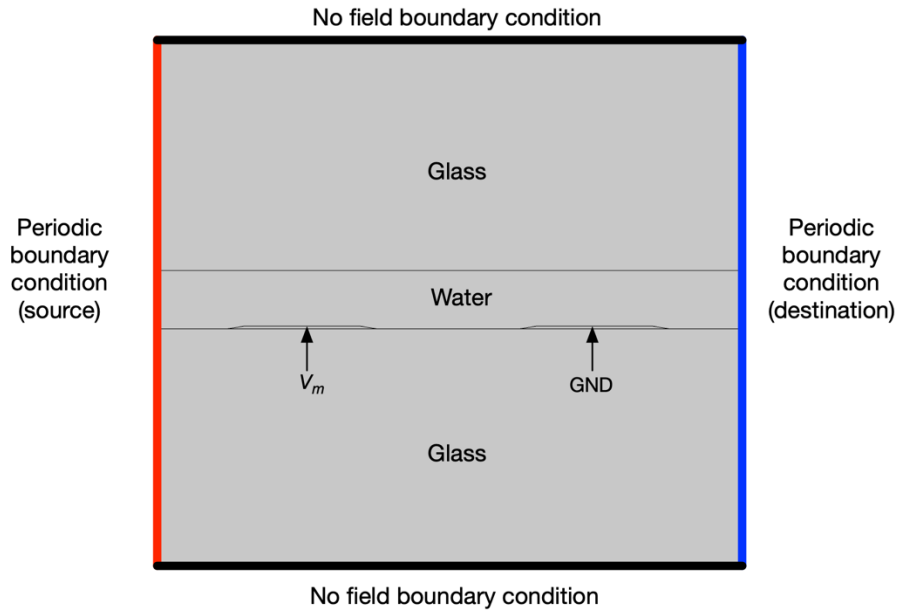


**Figure S3 Geometry of Region used for Finite Element Simulation.** The two dimensional region is  $50\text{ }\mu\text{m}$  wide and  $45\text{ }\mu\text{m}$  tall and corresponds to the region occupied by a single pair of electrodes.

These FEA simulations were also used to estimate  $R_m$  and  $C_m$ . Specifically, we estimate each of these values in separate calculations. For instance,  $R_m$  was calculated by setting the medium conductivity equal to  $\sigma_m$ , applying a set bias  $V_m$  across the electrodes, and using 2D stationary electrostatics simulation to compute the quasistatic current per unit depth  $i$  (a current per unit depth is calculated because this is a 2D simulation). Thus, to convert this value to a resistance, we employ the formula  $R_m = V/(niL)$ , where  $n = 10$  is the number of electrode pairs

in the device and  $L = 200 \mu\text{m}$  is the length of each electrode pair. To calculate  $C_m$ , the medium conductivity was set to 0 and the permittivity was set to  $\epsilon_m$ . Subsequently, FEM was used to compute the quasistatic capacitance per unit depth  $c$ , which led to the definition  $C_m = cnL$ . By independently calculating the frequency independent values of  $C_m$  and  $R_m$ , the complex medium impedance may be predicted at any frequency. Note that this analysis assumes that the voltage on the electrode matches the voltage in the bulk, which is often not the case due to electrode polarization. This factor is captured by our lumped element model through the electrode polarization capacitance  $C_e$  described in Equation (S3). The lumped element values of these terms are given in Table S1.

	<b>4×BB</b>	<b>1×BB</b>	<b>0.5×BB</b>	<b>0.25×BB</b>	<b>0.0625×BB</b>
<b>Borate conc. (mM)</b>	200	50	25	12.5	3.125
<b>Conductivity, <math>\sigma_m</math> (<math>\mu\text{S/cm}</math>)</b>	2420	1210	605	303	76
<b>Debye length, <math>\lambda_D</math> (nm)</b>	0.7	1.4	2.0	2.8	5.5
<b>Medium resistance <math>R_m</math> (k<math>\Omega</math>)</b>	18	71	142	285	1138
<b>Medium capacitance <math>C_m</math> (pF)</b>	75	75	75	75	75
<b>Electrode-solution capacitance <math>C_e</math> (nF)</b>	3.6	1.8	1.3	0.9	0.45

**Table S1. Electric conductivity of borate buffer (BB) solutions at different concentrations and associated lumped element circuit values of the measurement system.**

### ***Validation of Lumped Element Model***

To validate the lumped element calculation, the impedance of the fluid-filled microfluidic chamber was measured with an HP 4284A Precision LCR Meter at a working frequency of 1 MHz to match the operating frequency of the DEP experiment. Values estimated for these lumped element properties were found to be consistent with impedance measurements of the microfluidic chamber (Figure S4).

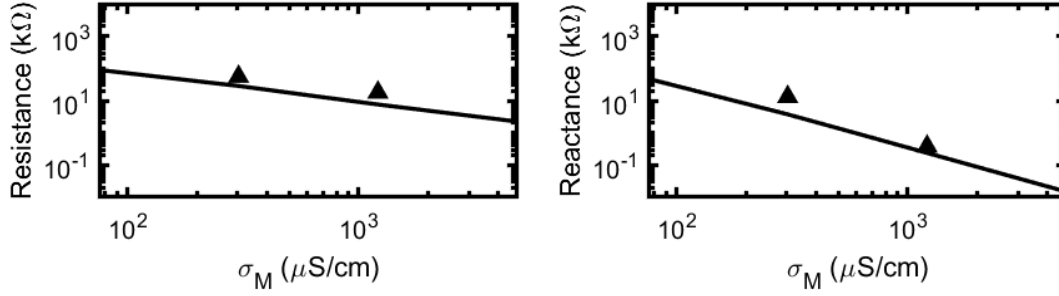


**Figure S4. Agreement between modeled and experimentally determined impedance.** The lumped element circuit model predicts a complex impedance  $Z$  in Equation (S1) that can be broken into its real (resistance) and imaginary (reactance) components. When evaluated at a frequency  $f = 1$  MHz, both of these terms are predicted to vary with medium conductivity  $\sigma_m$ . These calculations are shown as solid lines. These predictions are in agreement with the experimentally determined measurements of device-level resistance and reactance taken when the chamber was filled with two different buffers (black triangles). The experiments were performed at a 1 MHz operating frequency using an LCR meter.

### ***Determination of Working Frequency***

To determine the frequency range over which the applied voltage  $V$  approximately equals the voltage across the medium  $V_m$  without excessive (*i.e.*,  $> 1$  dB) losses to either electrode resistance (at high frequencies) or electrode polarization (at low frequencies), we evaluated the voltage distribution of the lumped element system using LTspice. Since these equations are linear, this allowed us to directly compute the ratio  $V_m/V$  vs.  $f$  with lumped element parameters chosen that correspond to different  $\sigma_m$ . The result of this analysis is that there is a window in  $f$  centered around 1 MHz for which  $V_m \approx V$ , thus motivating us to perform experiments at this frequency. This analysis further reveals that at frequencies that are too low, a substantial portion of the voltage is dissipated across  $C_e$  while at frequencies that are too high, a substantial portion of the voltage is dissipated across  $R_e$ . Delineating the boundaries of the working range as the points at which  $V_m = 0.9V$  (corresponding to a 1 dB loss in power), we define a working frequency for any given experimental condition (Figure 2E). It is important to note that the chosen operating frequency of 1 MHz is at minimum two decades from this boundary in all cases, making it highly unlikely that

slight adjustments to estimates of lumped element parameters will change the validity of this analysis.

Dissipating electrical power could, in principle, affect our measurement. In order to estimate the temperature increase in the fluid cell, we evaluated the limiting case of the largest applied voltage ( $\sim 3$  V) and the highest medium conductivity (resulting in a device resistance of 20 k $\Omega$ ). Under these conditions, we find that approximately 0.2 mW will be dissipated in the device. Given that most of this heat dissipation occurs in a  $200 \times 200$   $\mu\text{m}^2$  region of the fluid cell, we may estimate a worst case scenario and assume that the heat only escapes through the 100  $\mu\text{m}$  thick glass cover slip. Under these conditions, a temperature difference of 0.4  $^{\circ}\text{C}$  is all that is necessary to maintain steady state transport of heat out of the device. Given the miniscule scale of 0.4  $^{\circ}\text{C}$  relative to room temperature, we may safely neglect this factor when computing properties using the temperature. It is also worth mentioning that normalizing the QD intensity relative to a local background during every measurement removes the potential complication of QD brightness changing with temperature, even if the temperature swing was substantial.

## **2.2. Quantifying Concentration and Polarizability**

Having clarified the relationship between the applied voltage and the local electric field generated, the next step is to determine the local concentration and use this to estimate QD polarizability. This process involves two steps: (1) measuring the local concentration by quantifying local photoluminescence intensity and (2) converting this to a measure of concentration enhancement.

### ***Proportionality between Fluorescence Intensity and Local Concentration***

It is important to connect the fluorescence intensity  $I$  measured in terms of counts to the concentration  $C$ . We note that  $C$  varies in three dimensions (*i.e.*  $x$ ,  $y$ , and  $z$ ) while our fluorescence microscopy technique only allows us to interrogate  $I$  in two dimensions (*i.e.*  $x$  and  $y$ ). Thus, we interpret measurements of  $I$  by assuming that they represent averages of  $C$  as defined by  $I(x, y) \propto \int C(x, y, z) dz$ . This analysis is justified by the spatial resolution of the microscope. Specifically, for the 20 $\times$  objective used in this study (MPLN20XBD) with a numerical aperture (NA) of 0.4 imaging the 642 nm center wavelength of QD emission, one would expect a lateral resolution of  $\sim 800$  nm given by the width of Airy disc corresponding to the microscope point sampling function.<sup>6</sup> Importantly, the electrode array has features on the order of 10  $\mu\text{m}$  or more, indicating that the  $C$  profile will not appreciably vary on this scale. While this implies that the resolution is high at the focal plane, out-of-plane light can potentially limit our ability to usefully connect a 2D  $I$  map to a 3D  $C$  profile. However, a major reason why we chose to study QDs in microscopic channels is that it limits the impact of out-of-plane light. For instance, the maximum half angle of observation is  $\sim 20^\circ$ , which when connected with the 5  $\mu\text{m}$  height of the channel, indicates that we will be collecting light from a cone that is at most  $\sim 2$   $\mu\text{m}$  wide in the channel. This point spread function is superposed on the electric field simulation shown in Figure 2C to illustrate that the field is effectively constant in this region.

In order to ensure that the fluorescence intensity was a measure of a static local concentration, we included controls to show that the experiments were performed within the linear intensity response range for the QDs (Figure S5) and confirming that measurements were recorded at equilibrium rather than under kinetic conditions (Figure S6). The fluorescence intensity  $I$  was

tested for linearity with respect to QD concentration by imaging 0, 15, 15, 50, and 100 nM QD solutions under the experimental conditions, absent the electric field.

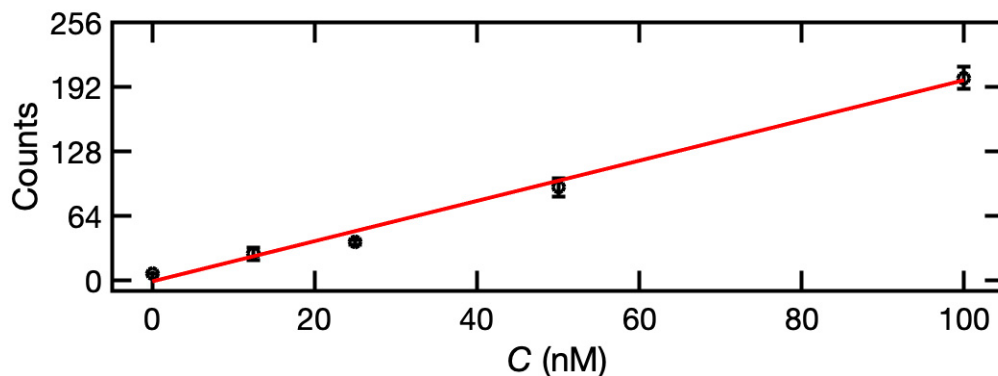


**Figure S5. Linear relationship between fluorescence intensity and QD concentration.** Fluorescence intensity  $I$  vs. quantum dot concentration  $C$  measured using a 500 nm excitation filter, a 642 nm emission filter, and a Hamamatsu ORCA R2 with 15 dB gain.

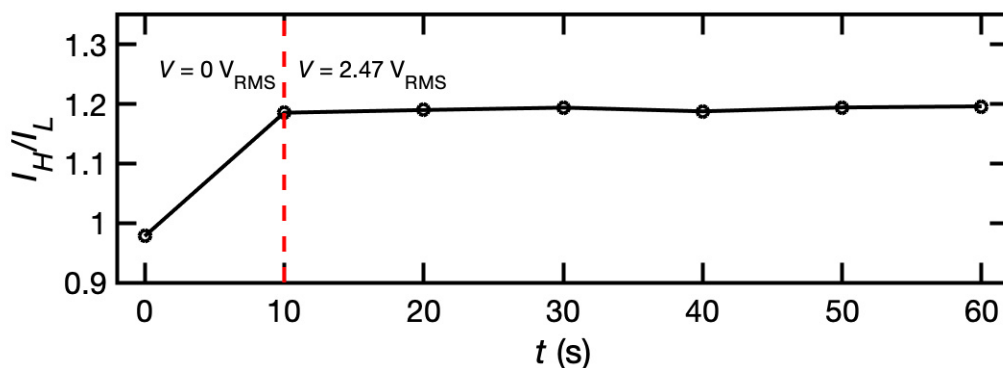


**Figure S6. Control for fluctuations in fluorescence intensity over time.** Fluorescence intensity in the high field region  $I_H$  normalized by intensity in the low field region  $I_L$  vs. time  $t$  with a voltage of  $V = 2.47$  V applied at  $t = 10$  s. The stability of this curve following the field being switched on indicates that the observed increase in concentration is not a kinetic effect.

### ***Fluorescence Assay to Measure Polarizability***

Before analyzing the local concentration  $C$ , one must acknowledge that the relatively long collection times and high gain associated with this type of imaging leads to an appreciable dark current. Thus, the value of the dark current  $I_{dark}$  (found by taking an image with the same imaging conditions but with the illumination source switched off) must be subtracted from the entire image.

Having recognized that  $C \propto I - I_{dark}$ , we note that  $E$  locally modifies  $C$  according to a Boltzmann distribution,

$$C = \frac{1}{Z} e^{\frac{\alpha E^2}{2k_B T}}, \quad (S6)$$

where  $Z$  is a normalizing factor known as the canonical partition function. Quantitative information cannot be obtained by only imaging a high field region because there is no guarantee that  $Z$  is constant as  $E$  is changing. Thus, a differential measurement is needed. To achieve this, we note that an electrode array is characterized by having a periodic array of high magnitude regions between the electrodes and low magnitude regions above the electrodes. Thus, we consider two locations, ‘High’ in which  $|E|$  is maximized and ‘Low’ where  $E = 0$ . If the system is in equilibrium, then  $C_L = \frac{1}{Z}$  while  $C_H = \frac{1}{Z} e^{\frac{\alpha E^2}{2k_B T}}$ . Thus, their ratio is expected to not depend on  $Z$ . A given image captured at 20 $\times$  magnification contains 4 pairs of these electrodes (Figure 3E). Thus, we sought to use all available information to accurately obtain the concentration in the high field region relative to that in the low field region. To automatically evaluate the images for changes in concentration, a custom script written in MATLAB evaluates every micrograph and performs sinusoidal curve fitting along a series of lines perpendicular to the electrode array to find the periodicity defined by the electrodes. Based upon this fitting, the brightness value of the bright regions that correspond to high field magnitude regions  $I_H$  and dark regions that correspond to low field magnitude regions  $I_L$  were identified. Rather than using the value of an individual pixel for each of these regions, a 7 pixel $\times$ 7 pixel region was averaged to estimate each value of  $I_H$  and  $I_L$ .

In order to use  $I_H$  and  $I_L$  to estimate the polarizability  $\alpha$ , we take the ratio of neighboring values of  $I_H$  and  $I_L$  to compute the ratio,

$$\frac{C_H}{C_L} = \left\langle \frac{I_H - I_{dark}}{I_L - I_{dark}} \right\rangle. \quad (S7)$$



Specifically, this process normalizes a given high field region with the adjacent low field region. Importantly, evaluating the intensity ratios locally was found to minimize the impact of non-uniform illumination. Three such images were averaged per experimental condition. Despite this averaging,  $C_H/C_L$  was found to differ slightly from 1 at zero applied field (typically by  $\sim 2\text{-}5\%$ ). We attribute this to a potential slight gradient in the chamber thickness, non-uniform illumination, the difference in reflectivity of the ITO surface vs. the glass surface, and/or the  $\sim 3\%$  difference in chamber height in the regions above the electrodes and the region above the gap. While these factors cannot easily be differentiated, they all merely change the proportionality between  $I - I_{dark}$  and  $C$ , thus they can be accommodated by including a fitting parameter. Namely, we fit these experimental data to,

$$\frac{C_H}{C_L} = b e^{\frac{\alpha V^2}{2k_B T d_e^2}}, \quad (\text{S8})$$

where  $b \approx 1$  is a fitting parameter. The parameter  $d_e$  represents the effective electrode spacing and is found using finite element simulation of the electric field magnitude  $|\vec{E}|$  (Figure 2C). In particular, considering that the chamber has a maximum height  $h$ , we define the effective electrode spacing as,

$$\frac{V_m}{d_e} = \frac{\int_0^h |\vec{E}| dz}{h}. \quad (\text{S9})$$

In these experiments, we find  $d_e = 15.5 \pm 0.2 \text{ } \mu\text{m}$ . This value of  $d_e$  is in agreement with the  $15 \text{ } \mu\text{m}$  separation between the electrodes, showing a consistency between the effective electrode spacing used for analysis and the physical dimension of the device.

### **3. SUPPORTING REFERENCES**

1. Chern, M.; Nguyen, T. T.; Mahler, A. H.; Dennis, A. M., Shell Thickness Effects on Quantum Dot Brightness and Energy Transfer. *Nanoscale* **2017**, *9* (42), 16446-16458.
2. Ghosh, Y.; Mangum, B. D.; Casson, J. L.; Williams, D. J.; Htoon, H.; Hollingsworth, J. A., New Insights into the Complexities of Shell Growth and the Strong Influence of Particle Volume in Nonblinking “Giant” Core/Shell Nanocrystal Quantum Dots. *J. Am. Chem. Soc.* **2012**, *134* (23), 9634-9643.
3. Nasilowski, M.; Spinicelli, P.; Patriarche, G.; Dubertret, B., Gradient Cdse/Cds Quantum Dots with Room Temperature Biexciton Unity Quantum Yield. *Nano Lett.* **2015**, *15* (6), 3953-3958.
4. Di Corato, R.; Quarta, A.; Piacenza, P.; Ragusa, A.; Figuerola, A.; Buonsanti, R.; Cingolani, R.; Manna, L.; Pellegrino, T., Water Solubilization of Hydrophobic Nanocrystals by Means of Poly (Maleic Anhydride-Alt-1-Octadecene). *J. Mater. Chem.* **2008**, *18* (17), 1991-1996.
5. Castellanos, A.; Ramos, A.; González, A.; Green, N. G.; Morgan, H., Electrohydrodynamics and Dielectrophoresis in Microsystems: Scaling Laws. *J. Phys. D: Appl Phys.* **2003**, *36*, 2584–2597.
6. Born, M., E. Wolf Principles of Optics. *Pergamon Press* **1980**, *6*, 188-189.